



Mechanical strengthening and corrosion behavior of friction stir welded dual-phase Fe₅₀Mn₃₀Co₁₀Cr₁₀ high entropy alloy

Shulei Sun ^{a,b}, Li Zhou ^{a,b,*}, Zhaoxu Yang ^b, Linghang Ma ^b, Xiaoguo Song ^{a,b}

^a State Key Laboratory of Precision Welding & Joining of Materials and Structures, Harbin Institute of Technology, Harbin, 150001, China

^b Shandong Provincial Key Laboratory of Special Welding Technology, Harbin Institute of Technology at Weihai, Weihai, 264209, China



ARTICLE INFO

Keywords:

Friction stir welding
High entropy alloy
Microstructure
Mechanical properties
Corrosion behavior

ABSTRACT

This study explores the mechanical strengthening and corrosion behavior of friction stir welded joints in dual-phase Fe₅₀Mn₃₀Co₁₀Cr₁₀ high entropy alloy (HEA). The influence of microstructural evolution on the joint's mechanical properties was analyzed, along with an assessment of its corrosion resistance using electrochemical quantitative analysis. Additionally, the corrosion mechanisms of HEAs were explored by analyzing corrosion morphology. The results show that the nugget zone exhibits a low fraction of HCP phase, yet refined grains contribute to higher hardness compared to the base metal. The presence of multiple dislocations, HCP phases, and partially fine grains enhanced hardness in thermal-mechanical affected zone and heat affected zone, despite coarse grain does not favor hardness in these zones. Although fracture occurred in the heat affected zone due to inadequate inhibition of coarse grains on the crack propagation, the TRIP effect increased the joint's tensile strength to 97.1 % of the base metal. Reduced Mn segregation and grain refinement in the nugget zone promote the formation of thicker and more uniform passivation films, which exhibit superior corrosion resistance compared to the base metal. Conversely, a high fraction of HCP phase in the base metal elevated its tensile strength but reduced elongation by inducing high stress concentrations near phase boundaries. And the combined effects of component segregation, a high fraction of HCP phase, and bulk grain boundaries accelerate base material dissolution.

1. Introduction

The dual-phase high entropy alloy (DP-HEA) demonstrates potential for improved strength and ductility [1–3], rendering it a promising candidate for applications in nuclear energy and automotive sectors. However, the widespread use of nickel-containing alloys is constrained by their high cost [4]. In contrast, Fe-Mn-Co-Cr alloys offer a more economical alternative. The non-equimolar ratios of the alloy elements modify the stacking fault energy (SFE), facilitating the development of both FCC and HCP phases [5,6]. For instance, adjusting the ratios of Co, Cr, and Fe influences the alloy's microstructure, where increasing Fe content from 30 % to 50 % reduces SFE and enhances the volume fraction of HCP phase [7]. Similarly, variations in Mn content impact the alloy's phase composition; elevated Mn levels favor a single FCC phase structure, while reduced levels promote the formation of the HCP phase in the FCC matrix [3]. Notably, the Fe₅₀Mn₃₀Co₁₀Cr₁₀ HEA achieves a balanced enhancement of strength and plasticity through bidirectional transformations between FCC and HCP phases [8,9]. Moreover, higher

strain rates accelerate these phase transformations, whereas finer grain sizes inhibit martensite formation, thus enhancing the material properties [10,11]. During adiabatic shearing, the strain in the adiabatic shear zone induces the formation of twins in the Fe₅₀Mn₃₀Co₁₀Cr₁₀ HEA, and the temperature rise leads to the disappearance of the HCP phase [12].

To facilitate broader application of these alloys, understanding their weldability and corrosion resistance is essential. Fusion welding of DP-HEA typically results in grain coarsening and reduced mechanical properties due to high temperatures [13–15]. Friction stir welding (FSW), however, operates below the material's melting point, facilitating plastic deformation and creating fine equiaxed grains [16–19]. Therefore, it is particularly necessary to study the microstructure and properties of the FSW joint with DP-HEA. Previous studies have found that friction stir processing of Si containing DP-HEA leads to a markedly refined FCC phase dominant microstructure, which facilitates the transformation of FCC phase to twin and HCP phase during deformation. This mechanism can result in higher strength and work-hardening

* Corresponding author. State Key Laboratory of Precision Welding & Joining of Materials and Structures, Harbin Institute of Technology, Harbin, 150001, China.
E-mail address: zhou.li@hit.edu.cn (L. Zhou).

ability of the processed material [20,21]. Furthermore, in the FSW joint of Fe_{38.5}Mn₂₀Co₂₀Cr₁₅Si₅Cu_{1.5} DP-HEA, the samples of heat affected zone (HAZ) showed excellent improvements in strength and ductility compared to the base metal (BM) [22].

For engineering applications, corrosion resistance is also essential [23,24]. Free Ni and high Mn content Fe₅₀Mn₃₀Co₁₀Cr₁₀ HEA exhibit reduced corrosion resistance [25]. Studying the relationship between the alloy's microstructure and corrosion resistance is therefore especially important. Generally speaking, finer grains in DP-HEA can increase grain boundary density, facilitating Cr accumulation in the passivation film and thereby enhancing its stability and corrosion resistance [26]. Nevertheless, the effect of grain size on corrosion resistance varies across different studies. While some indicate degraded corrosion resistance with finer grains in single-phase HEA [27], others observe an initial increase followed by a decrease in metastable HEA as grain size increases [28]. This variability underscores the importance of microstructure on corrosion behavior for optimizing alloy performance in practical applications.

FSW induces distinct thermal and mechanical conditions in different zones of the joint—nugget zone (NZ), thermal-mechanical affected zone (TMAZ), and HAZ [29,30]. These zones develop varied microstructures that inevitably influence the corrosion resistance of the material. Despite this, research on the corrosion resistance of DP-HEA FSW joints remains limited. The role of the dual-phase fraction distribution after FSW and the fine-grained NZ on the corrosion behavior needs more study. Based on this, the study conducted FSW of Fe₅₀Mn₃₀Co₁₀Cr₁₀ HEA, investigating the influence of grain size and dual-phase fractions on joint mechanical properties post-welding. Subsequently, corrosion behavior of the joints was studied to elucidate the corrosion mechanism of DP-HEA, providing essential theoretical insights for enhancing alloy corrosion resistance. This work particularly emphasized the influence of microstructure across different zones on both mechanical properties and corrosion behavior. It also addresses the possibilities of improving these two aspects through microstructure adjustments.

2. Experimental procedure

2.1. Assembly of FSW

The cast HEA was subjected to a homogenization process at 1200 °C for 2 h following hot-rolling at 900 °C. Subsequently, a 2.8 mm thick HEA plate was prepared through water quenching and cutting. As shown in Fig. 1, FSW was performed using a W-25Re alloy tool featuring a 15 mm shoulder diameter and a smooth surface with a 5° concave angle. The tool's smooth conical pin measured 2.38 mm in length, with diameters of 5.8 mm at the root and 4.8 mm at the tip. The welding parameters included a rotation speed of 300 rpm, a travel speed of 50 mm/min, a tool tilt angle of 2.5°, and a plunge depth of 0.25 mm. FSW was

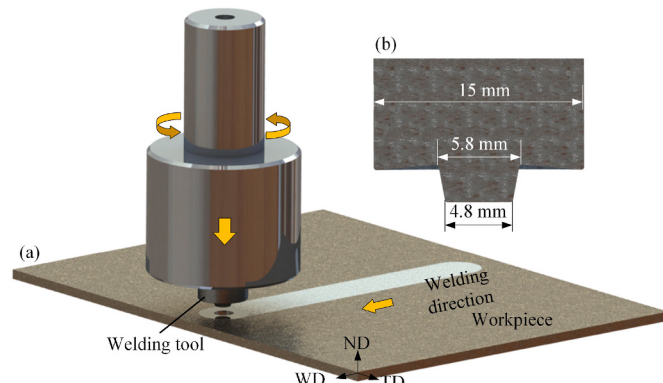


Fig. 1. Schematic of FSW Fe₅₀Mn₃₀Co₁₀Cr₁₀ HEA. (a) FSW process; (b) dimensions of welding tool.

conducted perpendicular to the rolling direction of the sheets.

2.2. Microstructure characterization and mechanical testing

Post-welding, metallographic samples were taken from the joint's cross-section for microstructure analysis. These samples underwent sandpaper and mechanical polishing, followed by chemical etching using a prepared solution (10 mL HCl, 10 mL C₂H₅OH, 0.25 g CuCl₂) to reveal NZ morphology. Optical microscope (OM) was employed for initial sample observation. For more detailed analysis, samples prepared for electronic backscattering diffraction (EBSD) testing underwent mechanical polishing and brief electrolytic corrosion in a 1:9 perchloric acid to alcohol solution at 25 V for 25 s. A Zeiss SIGMA500 scanning electron microscope (SEM) equipped with EBSD was utilized, with scanning step sizes ranging from 0.3 to 0.8 μm for both BM and FSW samples. Grain boundaries were categorized based on orientation angles: 2–15° as low angle grain boundaries (LAGB) and greater than 15° as high angle grain boundaries (HAGB). Phase analysis was performed using a DX-2700 X-ray diffraction spectrometer with Cu K α radiation, scanning from 30° to 110° at a scan speed of 0.02° s⁻¹, and operated at 45 kV and 200 mA under vacuum conditions.

A 2D hardness map of the weld section was generated using a Vickers hardness tester with a 500 g load and 10 s dwell time, measuring at 0.5 mm intervals horizontally and vertically. Three dog-bone-shaped samples were prepared for tensile testing at room temperature with a cross-head speed of 2 mm/min. Each sample measured a total length of 120 mm, a width of 12.5 mm, and a parallel section length of 50 mm. Subsequently, SEM analysis was conducted on the fracture surfaces of the tensile samples. Furthermore, the microstructure characteristics of TMAZ and fracture samples from FSW were examined using a FEI Talos F200S G2 transmission electron microscope (TEM). To prepare the TEM discs, samples with a diameter of 3 mm were first ground to a thickness of about 50 μm, followed by ion thinning at -35 °C and 30 V.

2.3. Electrochemical tests and immersion tests

Samples with size of 10 mm × 10 mm × 2.8 mm were cut from both the BM and WD-TD sections of joint. Copper wires were welded onto the bottom weld surface for etching. The analyzed area for testing was approximately 100 mm². After sealing the non-etched surfaces with epoxy resin, the sample's working face was ground and polished to achieve a mirror finish. For electrochemical characterization, a three-electrode setup was employed using a Zahner electrochemical workstation, with a saturated calomel electrode (SCE) as the reference electrode, a thin Pt plate as the counter electrode, and the sample itself as the working electrode. The open circuit potential (OCP) was determined, followed by electrochemical impedance spectroscopy (EIS) tests in a 3.5 wt% NaCl aqueous solution. Samples were immersed at room temperature for 3600 s to stabilize OCP measurements. EIS was performed across a frequency range of 10⁻¹ Hz–10⁵ Hz with an amplitude of 10 mV. Subsequently, polarization tests were conducted from -1.5 V to 0.5 V at a scan rate of 0.33 mV/s, and data were analyzed using CorrView software.

To examine corrosion across different weld zones (NZ, TMAZ, and HAZ), samples sized 10 mm × 20 mm were extracted from the weld center to the BM. Each sample underwent identical surface treatment before immersion in a 3.5 wt% NaCl solution for 12 and 24 h. Surface corrosion pits were measured using laser confocal microscopy, while SEM equipped with an energy dispersive spectrometer (EDS) was employed to study corrosion morphology and products.

3. Results and discussion

3.1. Microstructure characteristic

Fig. 2a illustrates cross-section images of the Fe₅₀Mn₃₀Co₁₀Cr₁₀ FSW

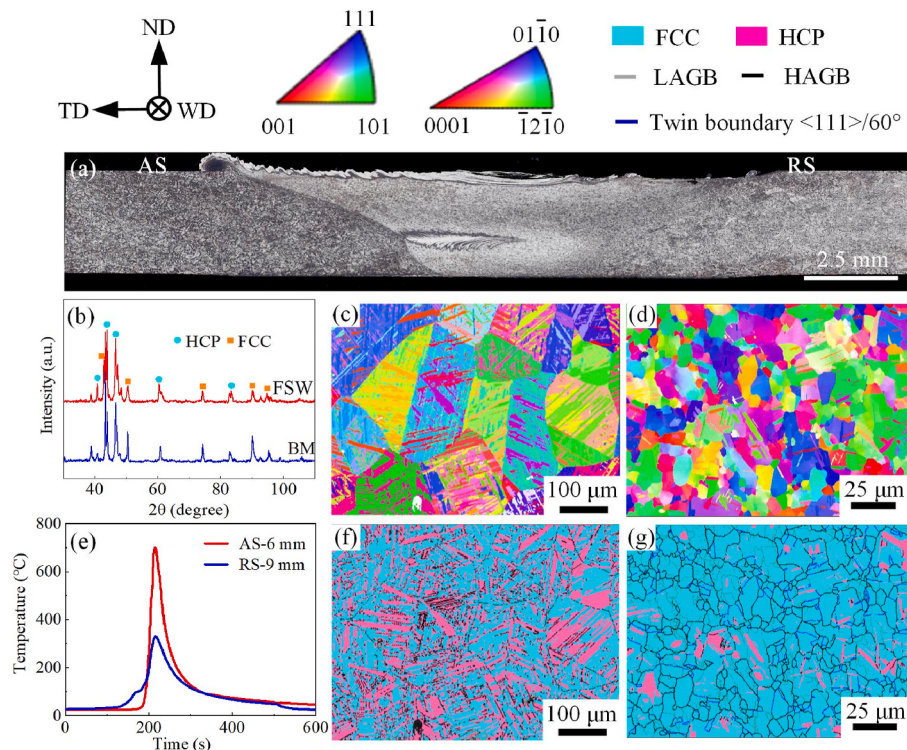


Fig. 2. Macro- and microstructure of $\text{Fe}_{50}\text{Mn}_{30}\text{Co}_{10}\text{Cr}_{10}$ FSW joint. (a) Cross-section morphology of weld at 300 rpm. (b) XRD analysis results of joint and BM. (c, d) EBSD IPF maps of FSW sample and BM, respectively. (e) Temperature evolution on the AS and RS during FSW. (f, g) Phase maps of FSW sample and BM, respectively. Note: AS is the advancing side, and RS is the retreating side.

joint, revealing a sound weld at 300 rpm with no voids in the NZ and unbind defects at the bottom of the weld. XRD results in Fig. 2b show FCC and HCP dual-phase microstructure of the alloy in the BM and the joint. The temperature evolution curves of AS and RS at 6 and 9 mm from the weld center, respectively, are displayed in Fig. 2e. It can be seen that the peak temperature exceeds the martensite transition temperature at both positions. EBSD analysis indicates grain refinement in the NZ compared to the BM, with a decreased volume fraction of HCP phase.

Quantitative analysis (see Fig. 3) shows that the BM comprises 5.1 % LAGB and 94.9 % HAGB, with 45.6 % FCC and 54.4 % HCP phases. After FSW, the proportion of LAGB in the NZ increases to 30.6 %,

accompanied by a decrease in HCP phase to 8.5 %. This phenomenon can be attributed to two primary factors: first, the high temperatures experienced during FSW promote the transformation of HCP phases in the BM to FCC phases [31]. Second, the fine grains in the NZ inhibit the regeneration of HCP phases from the FCC phase during the cooling. Nevertheless, the strain applied by the welding tool to the material still leads to the formation of FCC twins, as evidenced by the increase in the proportion of FCC twin boundary from 1.2 % in the BM to 21 % in the NZ in Fig. 3.

Microstructure distributions in the TMAZ and HAZ are illustrated in Fig. 4. OM images highlight severely deformed grains on the AS of TMAZ, clearly demarcating its boundary with the NZ. On the RS of TMAZ, a large number of fined grains are distributed around the coarse grains, with the distinct boundaries between TMAZ and NZ becoming less pronounced. DDRX emerges as the primary recrystallization mechanism in metastable DP-HEA with low stacking fault energy (SFE), as indicated by previous studies [32–34]. He et al. [10] calculated an SFE of 6.5 mJ m^{-2} at 300 K for the $\text{Fe}_{50}\text{Mn}_{30}\text{Co}_{10}\text{Cr}_{10}$ alloy, which led to the generation of small recrystallized grains via DDRX surrounding the coarse grains in the TMAZ (see Fig. 4d and e). Notably, fine grains characterized by a low martensite fraction are distinguished by a substantial presence of FCC twin boundaries, in contrast to coarse grains that do not recrystallize and instead exhibit a high proportion of lamellar martensite and a low proportion of twin boundaries. This observation suggests that dislocations and FCC twins serve as the primary mechanisms facilitating deformation in fine-grained microstructure.

Fine grains characterized by a low martensite fraction are distinguished by a substantial presence of FCC twin boundaries, in stark contrast to coarse grains, which do not undergo recrystallization and instead display a high proportion of lamellar martensite alongside a limited number of twin boundaries. This observation suggests that dislocations and FCC twins serve as the primary mechanisms facilitating deformation in fine-grained microstructures.

Moving further from the NZ into the HAZ, two significant trends

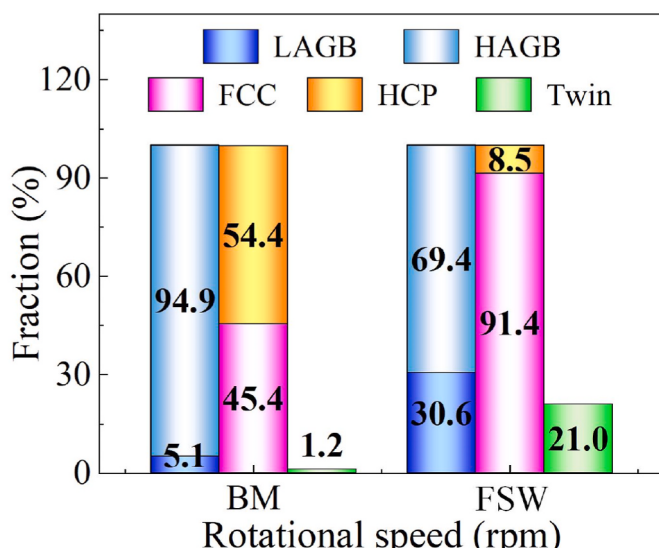


Fig. 3. Statistics on microstructural information of NZ and BM.

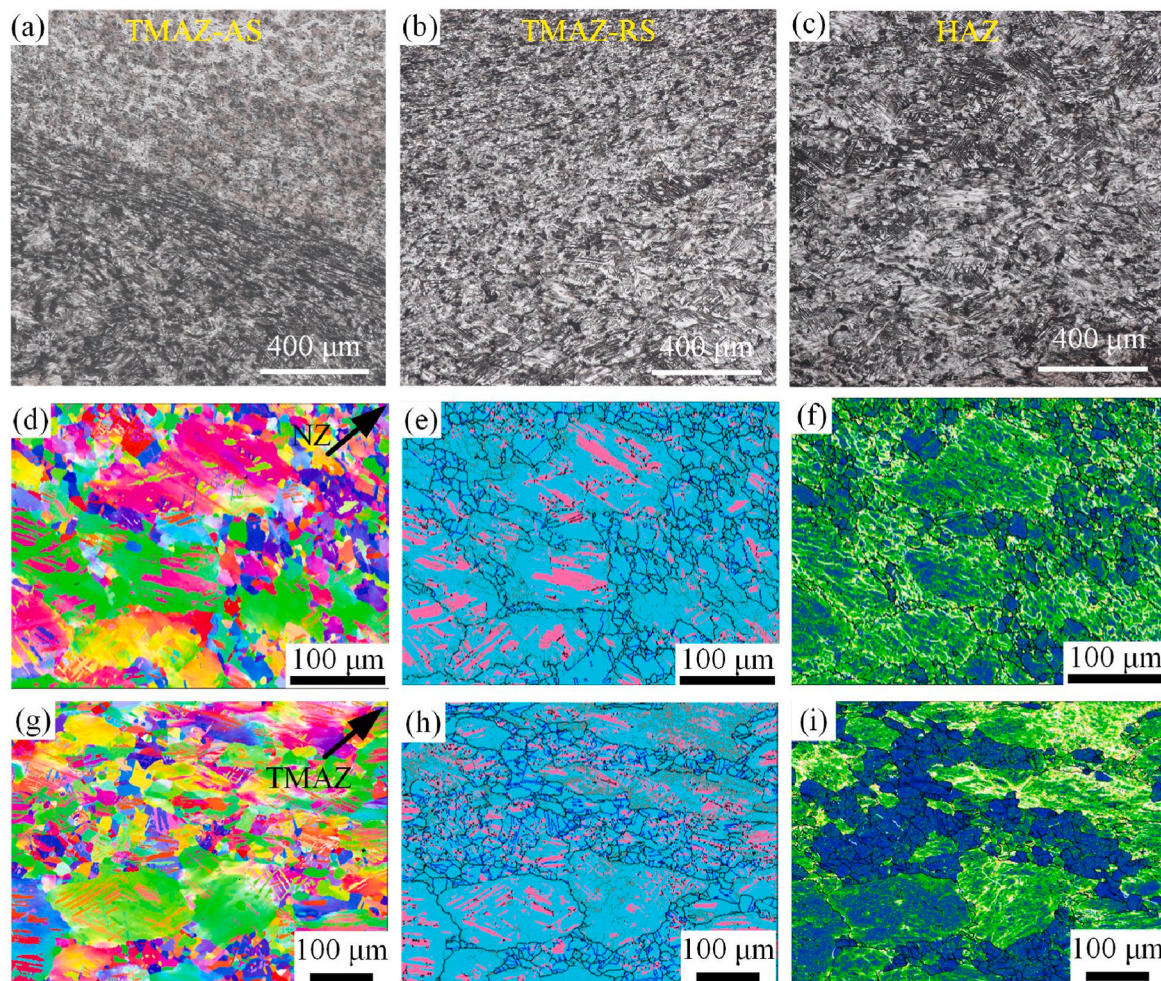


Fig. 4. Microstructure of FSW joint in different zones. (a–c) Optical micrograph of TMAZ-AS, TMAZ-RS, and HAZ, respectively. (d–f) EBSD IPF orientation mapping, phase map and KAM map of TMAZ, respectively. (g–i) EBSD IPF orientation mapping, phase map, and KAM map of HAZ, respectively.

emerge. Firstly, compared to the BM, the fraction of HCP phase in coarse grains without recrystallization is reduced, accompanied by a morphological shift from thick strips to lamellar structures (see Fig. 4g–h). This change suggests a combined influence of temperature and stress on the HCP phase in the HAZ. Secondly, there is a notable number of twin boundaries in the fine grains, and these fine grains exhibit a low density of geometrically necessary dislocations (GNDs). This phenomenon also appears in Fig. 4f. While the low SFE alloy typically favors the generation of HCP phases, the presence of finer grains impedes their transformation.

3.2. Microhardness and tensile behavior

The hardness distribution across the FSW joint is illustrated in Fig. 5. Notably, the joint exhibits enhanced hardness compared to the BM, except for a lower hardness zone at the bottom of the NZ. FSW typically enhances the hardness of HEA joints due to the refined grains in the NZ [19,22,30]. In the dual-phase Fe₅₀Mn₃₀Co₁₀Cr₁₀ FSW joint, the presence of a ceramic pad impedes the rapid heat diffusion during welding, resulting in localized heat accumulation at the bottom of the weld. This condition fosters grain growth and correlates with a reduced fraction of the HCP phase, which are primary contributors to reduced hardness. Despite the presence of coarse grains in the TMAZ and HAZ, a significant presence of dislocations, HCP phases, and partially recrystallized fine grains increases the hardness in these zones. Concurrently, a high hardness zone forms in RS of the joint.

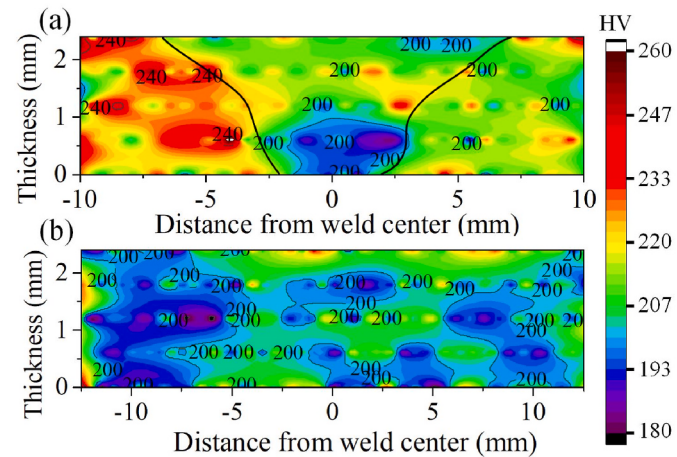


Fig. 5. Microhardness distribution on the BM and the Fe₅₀Mn₃₀Co₁₀Cr₁₀ joint. (a) FSW joint, (b) BM.

The stress-strain curves for the FSW sample and BM are illustrated in Fig. 6a. The results indicate that both the BM and FSW samples exhibit enhanced work-hardening ability due to the TRIP effect during plastic deformation. Notably, the BM sample demonstrates a higher ultimate tensile strength (UTS), while the FSW sample exhibits higher elongation

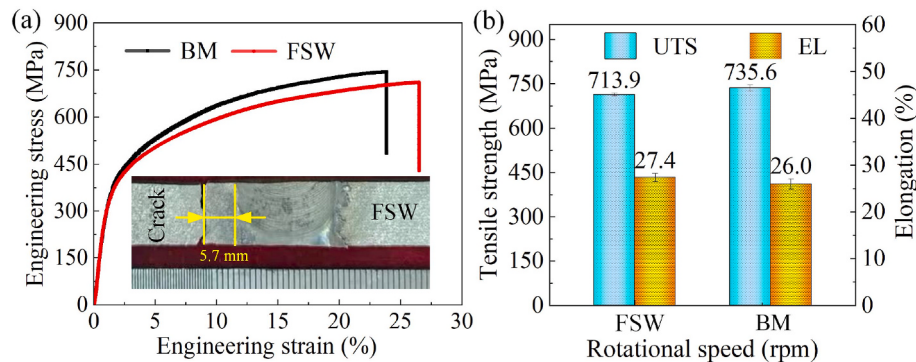


Fig. 6. The stress-strain curves (a) and transverse tensile properties (b) for the FSW sample and BM.

(EL). Fig. 6b shows the results of the tensile tests for both the joint and BM. The joint achieved an average UTS of 713.9 MPa, corresponding to 97.1 % of the BM. Moreover, the joint exhibited an average EL of 27.4 %, which is 105.4 % of the BM. Despite the lower hardness observed in the NZ of the joint welded at 300 rpm, the joint did not fracture in this softened zone. Analysis of Fig. 6b indicates that the fracture occurred 5.7 mm away from the weld edge on the RS of the joint. These results demonstrate consistent and commendable tensile properties of the joints produced under these welding parameters. The fracture morphology of the tensile sample is depicted in Fig. 7a–f. It is evident that the fracture pattern of the samples is predominantly characterized by dimples and quasi-cleavage planes, as indicated by the yellow and red arrows, respectively. Furthermore, particles are observed at the base of the dimples in the samples. The presence of these particles is likely to facilitate crack initiation during the tensile process, thereby compromising the tensile properties of the BM. Notably, the FSW sample displays a higher proportion of dimples compared to the BM, which exhibits more quasi-cleavage planes.

Fig. 8a and b presents the bright-field TEM images of FSW samples in TMAZ. Notably, a significant presence of HCP phases of varying widths is observed in the FCC matrix. These HCP phases can exhibit a staggered arrangement, facilitating the formation of different orientations. Fig. 8c further illustrates a high-resolution TEM (HRTEM) image at the

interface of the FCC and HCP dual phases, and they satisfy the orientation relationship of $\langle 110 \rangle_{\text{FCC}} // \langle 11 \bar{2} 0 \rangle_{\text{HCP}}$, $\{111\}_{\text{FCC}} // \{0002\}_{\text{HCP}}$ [35]. Additionally, numerous stacking faults (SFs) are observed in proximity to the interface. In the FCC matrix, away from the dual-phase interface, a large number of SFs also contribute significantly to the regulation of lattice distortion. Under appropriate strain conditions, these SFs can further transform into HCP phases, as depicted in Fig. 8d and e.

Subsequent TEM analysis was conducted on the FSW sample following uniaxial tensile testing, with the findings illustrated in Fig. 8f–j. Compared with the TMAZ samples prior to tensile testing, the dislocation density in the tensile samples is markedly elevated, accompanied by a proliferation of HCP laths in the grains. Furthermore, these HCP phases are characterized by a high density of dislocations, underscoring the pivotal roles of dislocation slip and HCP phase transformation in accommodating the strain experienced by the samples. A detailed analysis of the HCP phase tips indicates that the growth of the HCP phase in the width direction occurs progressively through the formation of a stepped structure. It is also noteworthy that HCP phases can nucleate simultaneously at various locations, resulting in the co-generation and gradual thickening of these phases, which collectively facilitate a coordinated response to the applied strain.

In summary, at the fracture position of the FSW sample, although the

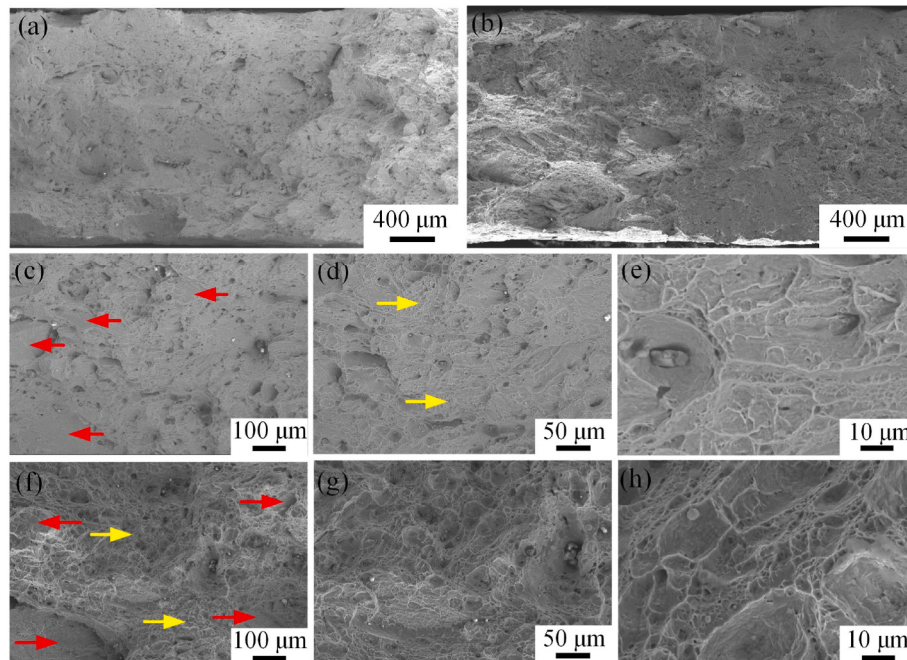


Fig. 7. Fracture morphology of the BM and FSW joint. (a, c–e) BM, (b, f–h) FSW sample.

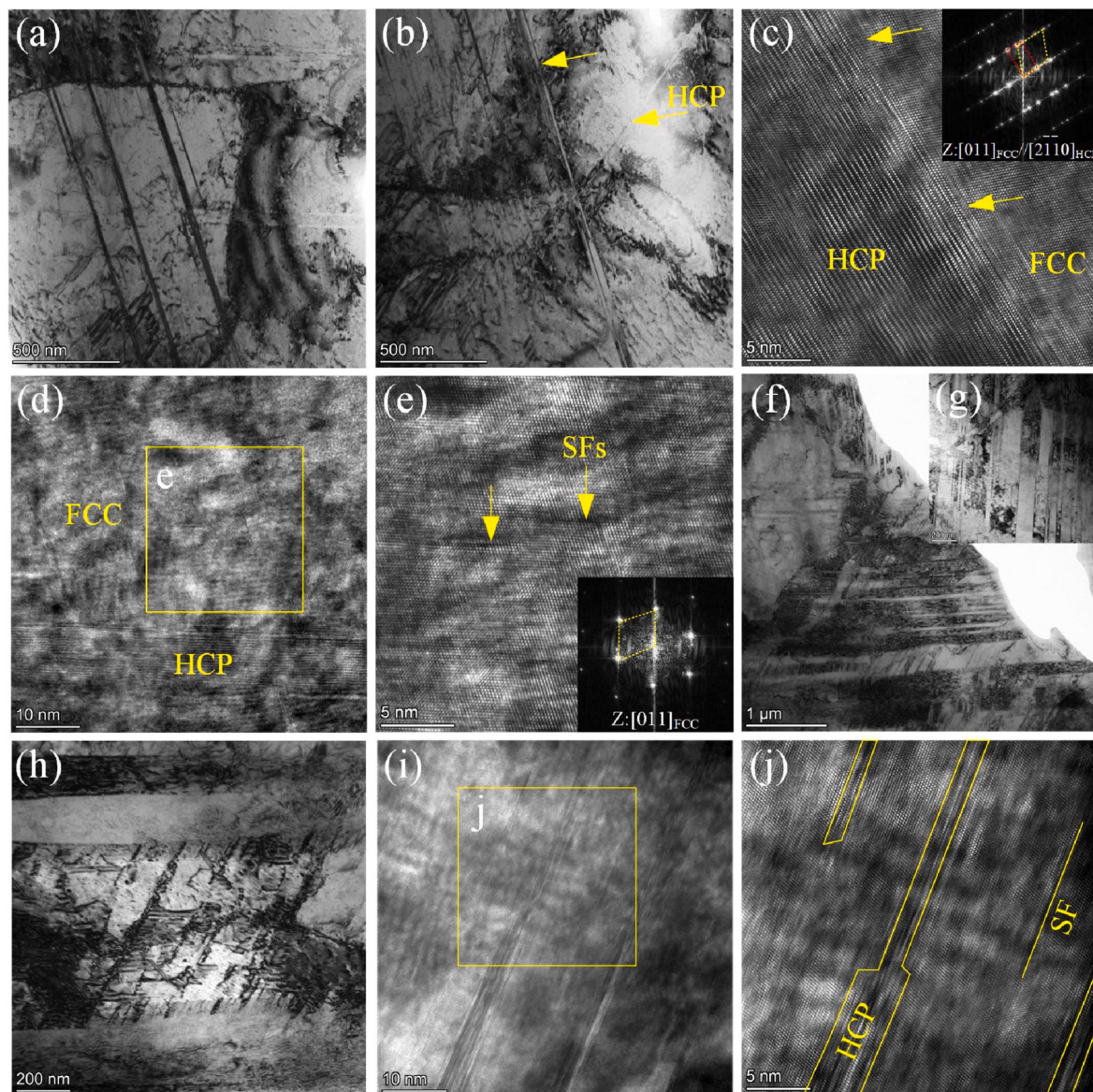


Fig. 8. TEM images of the FSW and fracture sample. (a, b) Bright-field TEM image of the FSW sample in the TMAZ; (c) HRTEM images of FCC and HCP phases; (d) HRTEM images of the FCC matrix, (e) enlarge view of the SFs in the FCC matrix. (f–h) Bright-field TEM image of the fracture sample; (i) HRTEM image of HCP phase tip; (j) enlarge view of zone j in (i).

microstructure enhances the joint's UTS through TRIP during tensile testing, its impact on joint strength remains limited. Coarser grains still facilitate crack propagation, resulting in decreased UTS. Conversely, the higher EL of welded joints compared to the BM suggests that the microstructure in the NZ plays a pivotal role in coordinating the deformation process. A higher fraction of FCC refined grains in the NZ contributes positively to EL. In contrast, HCP phase is widely distributed in the coarsened grains of the BM, where the large grain size exerts minimal resistance to the transformation from FCC to HCP phases during tensile testing. Due to the significantly greater hardness of the HCP phase compared to the matrix's FCC phase, higher tensile loads can be applied to HCP grains during the tensile process [36]. However, stress concentration near the phase boundary can easily lead to premature initiation and propagation of cracks, resulting in limited EL following fracture.

3.3. Electrochemical corrosion behavior

The grain size significantly impacts not just the mechanical

properties but also the corrosion resistance of the joint. Fig. 9a illustrates the OCP evolution for both BM and FSW samples in a 3.5 wt% NaCl solution over 3600 s. The OCP curves exhibit distinct behaviors between BM and FSW samples. Initially, there is a rapid decrease in OCP within the first 1200 s for the FSW sample, followed by relative stability with minor fluctuations until the end of testing. In contrast, the BM sample shows a slight increase in OCP during the first 600 s, followed by a reduction in volatility and stabilization around ~ 525 mV/SCE, markedly lower than the FSW sample. This indicates the progressive development and consistent interaction of the passive film with the solution [37]. The magnitude of OCP values serves as an indicator of the corrosion resistance of the passive film [38,39]. Importantly, higher OCP values on FSW samples signify the presence of a more protective passive film, thereby indicating superior corrosion resistance compared to the BM.

Potentiodynamic polarization (PDP) curves in Fig. 9b provide crucial insights into the evaluation of alloy corrosion resistance. The PDP curves for both FSW and BM samples exhibit a nearly overlapping trend in the cathodic branches, indicating minimal influence of grain size on

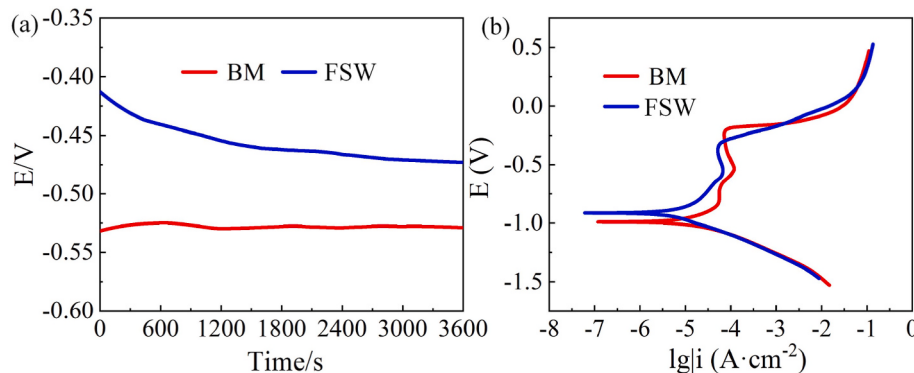


Fig. 9. The results of electrochemical measurements of the BM and FSW samples: (a) the OCP; (b) PDP tests of the BM and FSW samples.

cathodic reactions [40]. Accordingly, the corrosion potential (E_{corr}) for BM and FSW samples is -0.991 V_{SCE} and -0.915 V_{SCE}. Moreover, the corrosion current density (I_{corr}) values for BM and FSW samples in 3.5 wt % NaCl solution were approximately 8.61×10^{-6} A/cm² and 2.62×10^{-6} A/cm², respectively. Generally, lower I_{corr} values indicate greater stability and improved corrosion resistance due to reduced dissolution of the passivation film [41–43]. FSW sample showed higher E_{corr} and lower I_{corr} , which exhibits a lower dissolution rate and enhanced protective effect.

In the anodic branches, the passivation behavior in a 3.5 wt% NaCl solution demonstrates instability, as evidenced by fluctuations in the corrosion current density in response to increasing potential. Furthermore, the BM sample displays a higher corrosion current density throughout the passivation range compared to the FSW sample, despite the BM sample exhibiting wider passivation intervals and lower initial passivation potentials than the FSW samples. The breakdown potential (E_b) and passivation current density (i_{pass}) for BM are -0.225 Vsce and 7.28×10^{-5} A/cm², respectively, which are higher than the FSW sample. A smaller i_{pass} value indicates a denser and thicker passivation film [44]. The FSW sample displayed a lower i_{pass} value compared to the BM sample, indicating that its passivation film more effectively resists dissolution in chloride-rich environments. In summary, the microstructure characterized by fine equiaxed grains and a high fraction of FCC after FSW contributed to superior corrosion resistance compared to BM.

Fig. 10 presents Nyquist and Bode plots of BM and FSW sample under OCP conditions. In the Nyquist plot, all samples exhibit quarter-circle arcs, with larger diameters indicating better corrosion resistance due to enhanced stability of passivation film [45]. Comparatively, the BM sample exhibits a smaller capacitance curve radius than the FSW sample, implying superior corrosion resistance in the latter. The Bode plot in Fig. 10b reveals similar impedance modulus values at high frequencies ($\sim 10 \Omega \text{ cm}^2$), but notable discrepancies at lower frequencies ($\sim 2 \times 10^3 \Omega \text{ cm}^2$),

for FSW vs. $\sim 1.0 \times 10^3 \Omega \text{ cm}^2$ for BM). Furthermore, variations in phase angles indicate varied dissolution rates of the passivation films, with the FSW sample exhibiting enhanced charge impedance in chloride ion solutions.

An equivalent electric circuit (EEC) model depicted in Fig. 10a effectively simulates the inherent corrosion mechanisms in metastable HEAs. Previous research has reported a similar trend in Bode plots, confirming the presence of two time constants in impedance spectra consistent with EEC simulations [28]. Due to a difference between the impedance spectrum capacitance value of the corrosion system and ideal capacitance, constant phase elements (CPE) are employed instead of pure capacitors to compensate for this deviation [46,47]. The fitting results from ZsimDemo software presented in Fig. 10 and Table 1, demonstrating a high degree of concordance ($\chi^2 \approx 1 \times 10^{-4}$) between experimental and simulated Nyquist plots, thereby supporting the hypothesis of a dual-layer passivation film structure in Fe₅₀Mn₃₀Co₁₀Cr₁₀ HEAs immersed in NaCl solution. The parameter n , which reflects the uniformity of the passivation film [48,49], falls within the range of 0.5–1 for all dual-phase HEA samples. This range suggests an uneven distribution of the passivation film across the alloy surface [50]. This uneven distribution results in intermediate impedance behavior, reflecting characteristics between Warburg impedance and pure capacitance [51,52]. Table 1 also indicates that the resistance R_f of the external passivation film is lower than the impedance of the internal passivation film R_{ct} . This indicates that the corrosion resistance of the alloy's passivation film is primarily influenced by the inner dense passivation film, while the relatively inferior corrosion resistance of the outer passivation film may be attributed to its increased porosity. Notably, both R_{ct} and n_{ct} values for FSW samples exceed those of BM samples, indicating a more uniform, dense distribution of passive film and stronger corrosion resistance in the FSW sample.

Fig. 11 illustrate the surface morphology of both the BM and FSW samples after electrochemical corrosion. The FSW sample exhibits

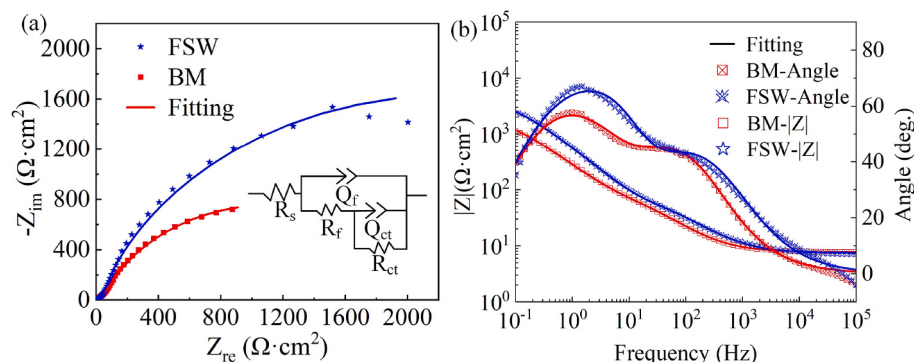


Fig. 10. Nyquist (a) and Bode (b) plots of the FSW and BM sample.

Table 1Fitting parameters of the EIS curves for the Fe₅₀Mn₃₀Co₁₀Cr₁₀ HEAs.

Sample	R_s ($\Omega \cdot \text{cm}^2$)	CPE_{f1}		R_f ($\Omega \cdot \text{cm}^2$)	CPE_{f2}		R_{ct} ($\Omega \cdot \text{cm}^2$)
		Q_f ($\text{k}\Omega^{-1} \cdot \text{cm}^{-2} \cdot \text{s}^\alpha$)	n_f		Q_{ct} ($\text{k}\Omega^{-1} \cdot \text{cm}^{-2} \cdot \text{s}^\alpha$)	n_{ct}	
BM	$7.75 \pm 0.6\%$	$0.40 \pm 7.8\%$	$0.76 \pm 1.4\%$	$105.6 \pm 9.8\%$	$0.48 \pm 7.2\%$	$0.80 \pm 2.1\%$	$2084 \pm 3.5\%$
FSW	$7.32 \pm 1.1\%$	$0.29 \pm 11.3\%$	$0.73 \pm 1.8\%$	$109.4 \pm 14.9\%$	$0.11 \pm 22.6\%$	$0.95 \pm 4.2\%$	$4556 \pm 6.2\%$

Note: resistance of solution (R_s), passive film resistors (R_f), capacitors with loose external structures (Q_f), charge transfer resistance (R_{ct}), capacitors with dense internal structures (Q_{ct}). CPE_{f1} and CPE_{f2} are R_f and R_{ct} constant phase angle elements, respectively.

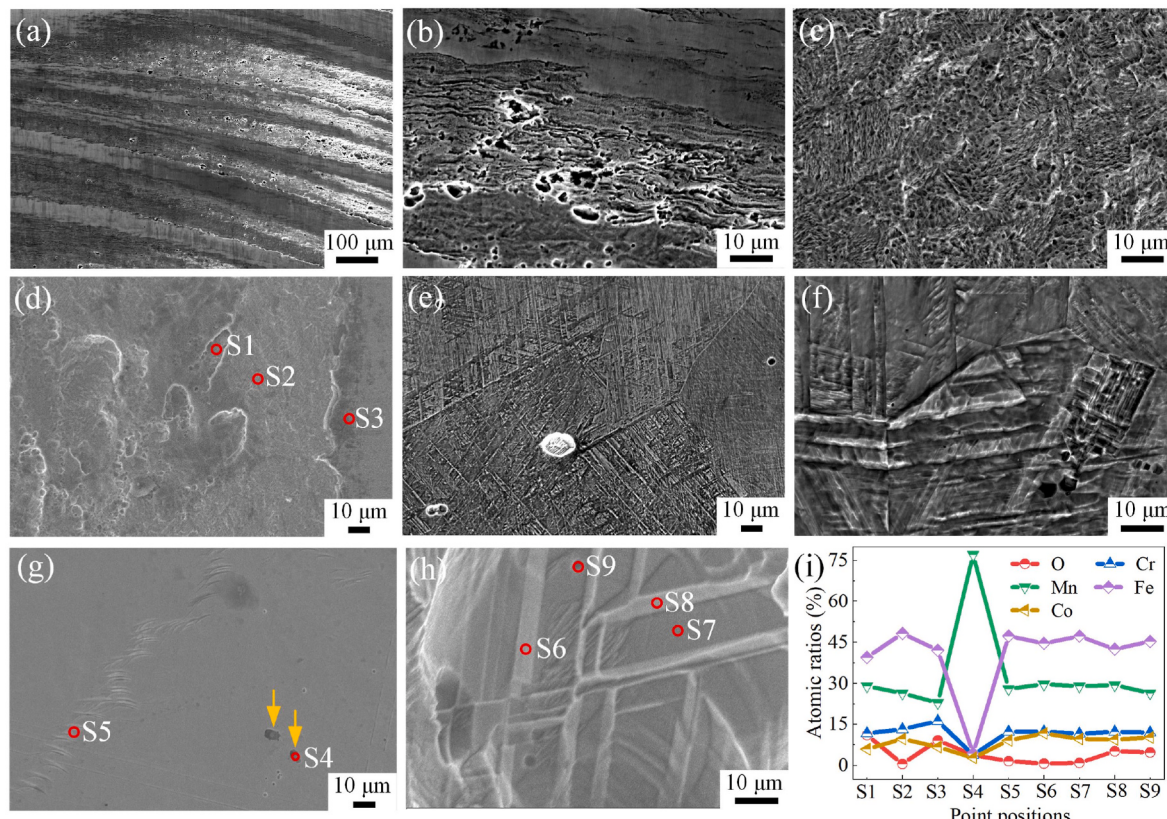


Fig. 11. Electrochemical corrosion morphologies of the samples were characterized by SEM technology. (a–d) FSW samples, (e–h) BM. EDS analyzed the components at different positions of the sample, the results are shown in (i).

distinct traces attributable to the rotational shoulder (see Fig. 11a). Microscopically, the surface of the FSW weld displays arc patterns characterized by periodic distributions of fine and coarse grains [53]. Areas with finer grains are particularly susceptible to corrosion, as evidenced in Fig. 11b and c. Fig. 11e, f shows significant preferential corrosion at grain boundaries and phase boundaries in the BM. Typically, corrosion pits initiate preferentially at surface defects such as grain boundaries and local stress concentration regions, significantly impacting material corrosion resistance [46]. Additionally, EDS was used to analyze element distribution in various positions of both BM and FSW sample. The corroded surface of the FSW sample predominantly exhibits a passivation film composed of oxides, with certain regions revealing unoxidized metal (see Fig. 11d–i). In contrast, the BM sample contains segregated Mn particles, identified as preferred sites for corrosion initiation (see S4 in Fig. 11g–i). Furthermore, Fig. 11h illustrates that the FCC matrix and HCP martensite exhibit no discernible tendency for preferential passivation film formation following film removal.

3.4. Immersion corrosion behavior and corrosion mechanism

To further research the corrosion mechanisms, both the BM and welded Fe₅₀Mn₃₀Co₁₀Cr₁₀ HEA samples were immersed in a 3.5 wt% NaCl solution for 12 and 24 h. Fig. 12 displays the distribution of corrosion pits on the sample surfaces after immersion. After 12 h, corrosion sites on the welded sample are primarily located inside the NZ, shifting to its periphery after 24 h. Laser confocal scanning of these corrosion pits in Fig. 12 reveals preferential growth at specific sites. Notably, the depth of corrosion pits on the welded sample (66.1 μm) is significantly less than that on the BM (84.6 μm).

Further investigation of the corrosion characteristics of both the FSW samples and BM was conducted using SEM and EDS. Typically, grain boundaries and triple points in the microstructure serve as preferential sites for initiating nucleation of passivation films. Fine-grained structures provide more nucleation sites compared to coarse-grained ones, facilitating denser passivation film formation [54]. Interestingly, the increased nucleation sites in the NZ of welded samples suggest superior corrosion resistance, despite initial stage corrosion being more pronounced due to grain boundary susceptibility [27]. SEM images of corrosion pits in FSW samples reveal preferential attack at phase and

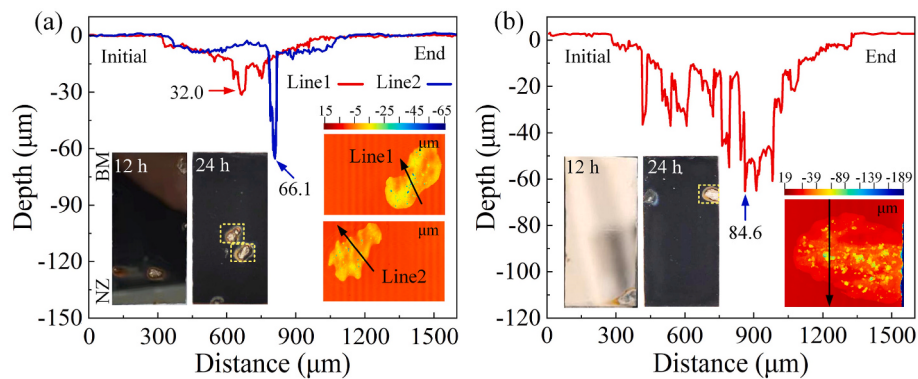


Fig. 12. Measurement results of corrosion pit depth in the FSW sample (a) and BM (b).

grain boundaries (see Fig. 13b and c), which is similar to electrochemical test results in Fig. 11. Weak adhesion between fragments and the matrix results in detachment of corrosion products from the material surface over time. This may be the reason for the fluctuations in the passivation behavior of the PDP curve in the anode branches (see Fig. 9b).

Previous research has found that passivation films formed by Fe₅₀Mn₃₀Co₁₀Cr₁₀ in chloride solutions exhibit high concentrations of Fe and Mn, with comparatively lower levels of Cr [55]. SEM mapping in Fig. 13d, e confirms that corrosion fragments predominantly consist of Cr-O rich phases. Similarly, the formation of a passivation film rich in Cr during the initial stages of corrosion in NaCl solution has been observed for FeMnCoCrNi HEA [27]. As corrosion progresses, the passivation film gradually deteriorates, exposing fresh metal surfaces beneath.

Analysis of SEM maps of BM revealed that its corrosion surface showed more signs of exposed metal corrosion without visible peeling of the passivation films. Further EDS analysis in Fig. 14a and b identified the distribution of oxygen elements on the corrosion surface, suggesting insufficient sites for the formation of a passivation film in the coarse grains of BM. As a result, the passivation film in the BM exhibits inferior thickness, uniformity, and consistency compared to that of the FSW samples. This observation is further supported by the electrochemical test results presented in Figs. 9 and 10. Moreover, the substantial fraction of HCP phase in BM accelerates the corrosion of the material.

Element segregation, particularly Mn-rich precipitates, significantly contributes to corrosion susceptibility, leading to localized pitting corrosion as depicted in Fig. 14d and e. Studies by Nene et al. [56] indicate that corrosion behavior is more influenced by particle distribution than selective attacks along grain boundaries in chloride solutions. Throughout the corrosion process, Mn-rich phases become exposed to the corrosive environment, gradually detaching from the matrix and forming circular pits on the metal surface. These results are consistent with earlier research that found Mn to be an alloying element that reduces corrosion resistance and encourages pitting corrosion at lower potentials [57,58]. Therefore, the combined effect of component segregation, a high fraction of HCP phase, and bulk grain boundaries accelerates alloy dissolution of BM.

For Fe₅₀Mn₃₀Co₁₀Cr₁₀ DP-HEA, coarse grains in BM facilitate a uniform distribution of FCC and HCP phases. In tensile tests, coarse grains exhibit minimal resistance to the transformation from FCC to HCP phases. The harder HCP martensite bears higher tensile loads, prematurely initiating and propagating cracks, ultimately leading to fracture while decreasing EL. Concurrently, material composition and microstructural attributes exert significant influence on corrosion resistance [59,60]. Segregation of Mn phases in BM favors the occurrence of pitting corrosion. At the same time, the high fraction distribution of HCP phases in the BM increases the density of phase boundary. Elevated electrochemical potentials at these phase boundaries accelerate passive film

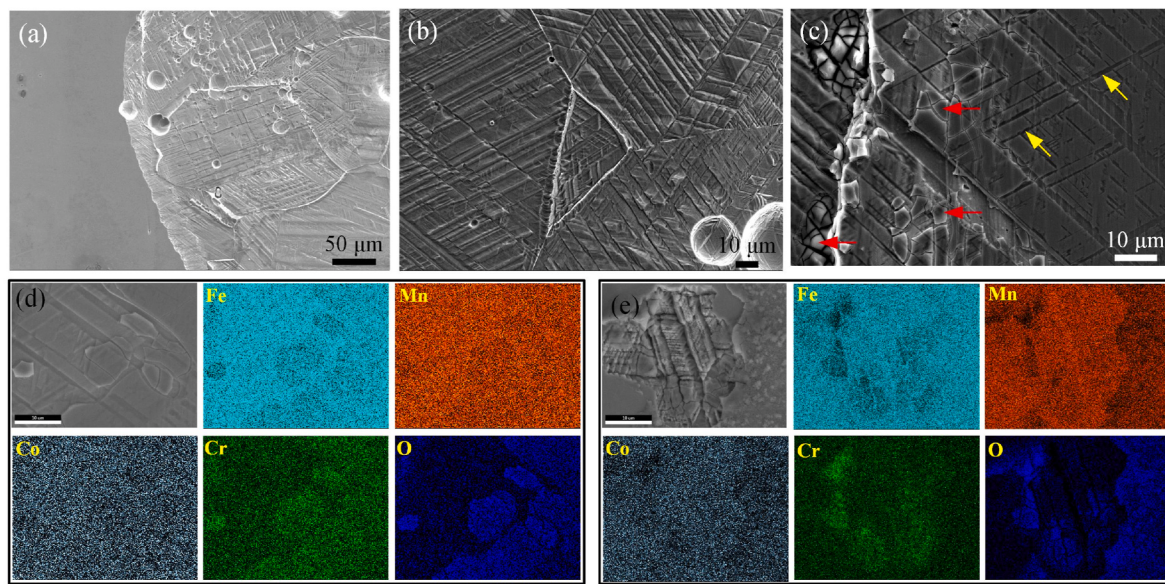


Fig. 13. Photographs of FSW samples after 24 h of immersion in a 3.5 wt% NaCl solution. (a–c) Corrosion morphology of welded joint after immersion. (d, e) EDS maps for the fragments and corrosion pit, respectively.

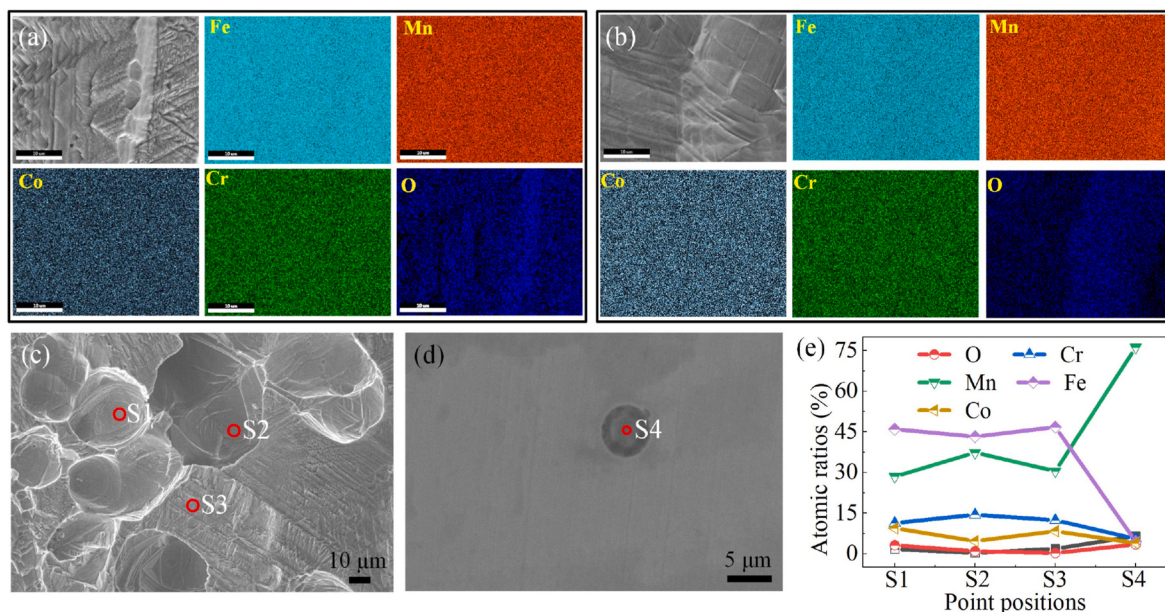


Fig. 14. Photographs and EDS results of BM samples after 24 h of immersion in a 3.5 wt% NaCl solution. (a, b) EDS maps for the corrosion surface. (c, d) SEM image capturing the corrosion pits on the corrosion surface. (e) EDS results from positions S1-S4.

dissolution. Larger grain sizes reduce the density of grain boundaries, which decreases susceptibility to grain boundary corrosion. However, this reduction also results in uneven distribution and thinning of the passivation film, which can facilitate localized corrosion along grain and phase boundaries. Consequently, this undermines the protective efficacy of the passivation film on the metal surface.

The NZ of the FSW joint exhibits a refined grain structure compared to the BM, and a much lower fraction of HCP phase. While thermal accumulation at the lower portion of the NZ leads to a slight decrease in hardness, other zones in the NZ experience increased hardness due to grain refinement. In TMAZ, the observed enhancement in hardness can be attributed to increased dislocation densities, partial grain recrystallization, and HCP phase retention from the BM. The FCC refined grains in NZ and TRIP effect positively influences the EL of the joint. Conversely, coarse grains in HAZ and a higher fraction of HCP phase can facilitate the initiation and propagation of cracks during tensile loading, ultimately leading to joint failure in this zone. In contrast, the presence of coarse grains in HAZ, coupled with a higher fraction of the HCP phase, promotes the initiation and propagation of cracks during tensile loading, ultimately leading to joint failure in this region.

The elevated proportion of face-centered cubic (FCC) refined grains in the nugget zone (NZ) and the transformation-induced plasticity (TRIP) effect positively influence the elongation (EL) of the joint. In contrast, the presence of coarse grains in the heat-affected zone (HAZ), along with a higher fraction of the HCP phase, tends to promote crack initiation and propagation during tensile loading, ultimately leading to joint failure in this region. On the other hand, FSW joints reduced the distribution of HCP phase in the NZ, resulting in fewer phase boundaries. This characteristic promotes the rapid formation of a uniform passive film on the surface. Moreover, tool stirring during FSW ensures a more uniform distribution of Mn particles in the NZ microstructure, enhancing its resistance to pitting corrosion in chloride ion environments. Fig. 15 shows the schematic diagram of the corrosion.

4. Conclusion

1. The welding temperatures and fine grains decrease the fraction of HCP phase in the NZ, while the presence of several FCC twins coordinates strain accumulation. In TMAZ and HAZ, the FCC twins are

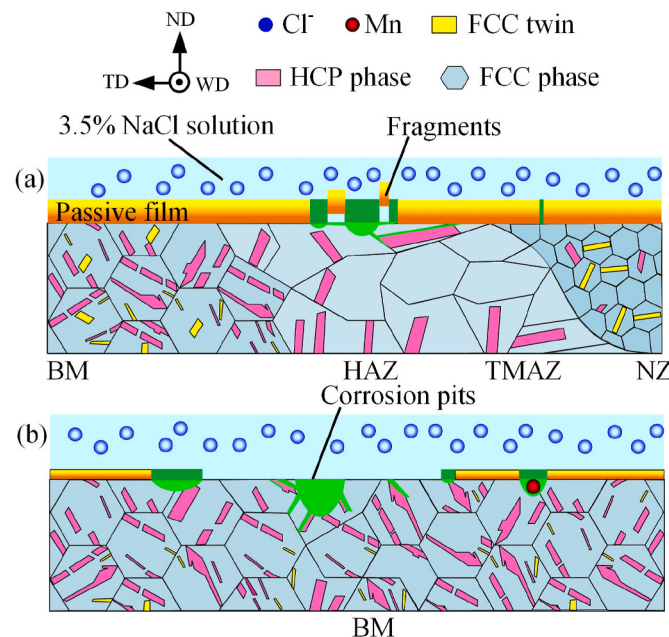


Fig. 15. Schematics showing corrosion mechanism of FSW joint and BM in the NaCl solution.

- mainly distributed in the fine grains with low density of GNDs, whereas the HCP phase is mainly distributed in the coarse grains.
2. Except for localized softening present at the bottom of the NZ, the hardness at other regions in the NZ is higher compared to the BM due to grain refinement. In both TMAZ and HAZ, the increased hardness is attributed to the presence of dislocations, HCP phases, and partially recrystallized fine grains, despite the coexistence of coarser grains.
 3. The UTS and EL of the joint reach 97.1 % and 105.4 % of the BM, respectively. Fracture initiation occurs in HAZ of the joint, where coarser grains offer less resistance to crack propagation, resulting in reduced UTS. Conversely, the high fraction of HCP phase in the BM increases the UTS but also promotes stress concentration near the

- phase boundary, facilitating early crack initiation and reducing EL post-fracture.
4. The NZ microstructure exhibits higher corrosion resistance compared to the BM, primarily due to reduced Mn segregation and the acquisition of refined grains, which promotes the formation of a thicker and more uniform passive film. And the lower proportion of phase boundaries in the NZ reduces susceptibility to corrosion. However, the combined effects of component segregation, a higher fraction of HCP phase, and bulk grain boundaries accelerate the dissolution of the BM.
- CRediT authorship contribution statement**
- Shulei Sun:** Writing – review & editing, Writing – original draft, Visualization, Formal analysis, Data curation, Conceptualization. **Li Zhou:** Writing – review & editing, Supervision, Funding acquisition, Formal analysis. **Zhaoxu Yang:** Visualization, Methodology, Investigation, Data curation. **Linghang Ma:** Writing – original draft, Visualization, Investigation, Data curation. **Xiaoguo Song:** Writing – review & editing, Validation, Supervision, Funding acquisition.
- Declaration of competing interest**
- The authors declare that they have no known competing financial interests or personal relationships that could have appeared to influence the work reported in this paper.
- Acknowledgements**
- This work was supported by the National Natural Science Foundation of China (No. 52375316 and 52175307) and Taishan Scholars Foundation of Shandong Province (No.tsqn 202211089).
- Data availability**
- Data will be made available on request.
- References**
- [1] Z.M. Li, C.C. Tasan, K.G. Pradeep, D. Raabe, A TRIP-assisted dual-phase high-entropy alloy: grain size and phase fraction effects on deformation behavior, *Acta Mater.* 131 (2017) 323–335.
 - [2] R. Jain, V. Parameswaran, K. Biswas, N.P. Gurao, Bidirectional transformation enabled improvement in strength and ductility of metastable $\text{Fe}_{50}\text{Mn}_{30}\text{Co}_{10}\text{Cr}_{10}$ complex concentrated alloy under dynamic deformation, *Int. J. Plast.* 166 (2023) 103633.
 - [3] Z.M. Li, K.G. Pradeep, Y. Deng, D. Raabe, C.C. Tasan, Metastable high-entropy dual-phase alloys overcome the strength-ductility trade-off, *Nature* 534 (7606) (2016) 227–230.
 - [4] Q.Z. Gao, Z.Y. Liu, L.L. Sun, Q.S. Ma, H.L. Zhang, J. Bai, X.P. Lin, L.M. Yu, H.J. Li, Review on precipitates and high-temperature properties of alumina-forming austenitic stainless steel, *J. Mater. Res. Technol.* 25 (2023) 5372–5393.
 - [5] Y. Xu, W.W. Xiong, T. Luo, R.R. Liu, S.Y. He, X.H. Zhu, S.P. Li, Z.H. Huang, Z. H. Liao, Twinning damping interface design and synergistic internal friction behavior in FeMnCrCo high-entropy alloys, *Mater Sci Eng A* 857 (2022) 144040.
 - [6] Z.M. Li, D. Raabe, Strong and ductile non-equiautomic high-entropy alloys: design, processing, microstructure, and mechanical properties, *JOM* 69 (11) (2017) 2099–2106.
 - [7] P. Singh, S. Picak, A. Sharma, Y.I. Chumlyakov, R. Arroyave, I. Karaman, D. D. Johnson, Martensitic transformation in $\text{Fe}_x\text{Mn}_{80-x}\text{Co}_{10}\text{Cr}_{10}$ high-entropy alloy, *Phys. Rev. Lett.* 127 (11) (2021) 115704.
 - [8] W.J. Lu, C.H. Liebscher, G. Dehm, D. Raabe, Z.M. Li, Bidirectional transformation enables hierarchical nanolaminate dual-phase high-entropy alloys, *Adv. Mater.* 30 (44) (2018) 1804727.
 - [9] Y.X. Liang, L. Zhang, C.Y. Bai, J.F. Zhao, L.B. Wang, W. Guo, J. Tu, Q. Wan, Bidirectional phase transformation facilitated by ϵ -martensite bands interaction in metastable $\text{Fe}_{50}\text{Mn}_{30}\text{Co}_{10}\text{Cr}_{10}$ dual-phase high entropy alloys, *Mater. Char.* 208 (2024) 113655.
 - [10] Z.F. He, N. Jia, H.W. Wang, Y. Liu, D.Y. Li, Y.F. Shen, The effect of strain rate on mechanical properties and microstructure of a metastable FeMnCoCr high entropy alloy, *Mater Sci Eng A* 776 (2020) 138982.
 - [11] Y. Liu, J. Tu, L. Deng, C.H. Wang, Z.M. Zhou, Z.T. Jiang, J.R. Luo, Characteristics of thermal- and strain-induced ϵ -martensite in $\text{Fe}_{50}\text{Mn}_{30}\text{Co}_{10}\text{Cr}_{10}$ multi-component alloy: effect of grain size, *Mater. Char.* 171 (2021) 110817.
 - [12] S.J. Yang, Y. Yang, Thermodynamics-kinetics of twinning/martensitic transformation in $\text{Fe}_{50}\text{Mn}_{30}\text{Co}_{10}\text{Cr}_{10}$ high-entropy alloy during adiabatic shearing, *Scripta Mater.* 181 (2020) 115–120.
 - [13] Z. Wu, S.A. David, D.N. Leonard, Z. Feng, H. Bei, Microstructures and mechanical properties of a welded CoCrFeMnNi high-entropy alloy, *Sci. Technol. Weld. Join.* 23 (7) (2018) 585–595.
 - [14] J.P. Oliveira, T.M. Curado, Z. Zeng, J.G. Lopes, E. Rossinyol, J.M. Park, N. Schell, F. M. Braz Fernandes, H.S. Kim, Gas tungsten arc welding of as-rolled CrMnFeCoNi high entropy alloy, *Mater. Des.* 189 (2020) 108505.
 - [15] H. Nam, C. Park, J. Moon, Y. Na, H. Kim, N. Kang, Laser weldability of cast and rolled high-entropy alloys for cryogenic applications, *Mater Sci Eng A* 742 (2019) 224–230.
 - [16] S. Park, H. Nam, J. Park, Y. Na, H. Kim, N. Kang, Superior-tensile property of CoCrFeMnNi alloys achieved using friction-stir welding for cryogenic applications, *Mater Sci Eng A* 788 (2020) 139547.
 - [17] X. Qin, Y. Xu, Y. Sun, H. Fujii, Z. Zhu, C.H. Shek, Effect of process parameters on microstructure and mechanical properties of friction stir welded CoCrFeNi high entropy alloy, *Mater Sci Eng A* 782 (2020) 139277.
 - [18] N. Xu, Q.N. Song, Y.F. Bao, Microstructure evolution and mechanical properties of friction stir welded FeCrNiCoMn high entropy alloy, *Mater. Sci. Technol.* 35 (5) (2019) 577–584.
 - [19] Z.G. Zhu, Y.F. Sun, F.L. Ng, M.H. Goh, P.K. Liaw, H. Fujii, Q.B. Nguyen, Y. Xu, C. H. Shek, S.M.L. Nai, J. Wei, Friction-stir welding of a ductile high entropy alloy: microstructural evolution and weld strength, *Mater Sci Eng A* 711 (2018) 524–532.
 - [20] S.S. Nene, M. Frank, K. Liu, R.S. Mishra, B.A. McWilliams, K.C. Cho, Extremely high strength and work hardening ability in a metastable high entropy alloy, *Sci. Rep.* 8 (1) (2018) 9920.
 - [21] S. Sinha, S.S. Nene, M. Frank, K. Liu, R.A. Lebensohn, R.S. Mishra, Deformation mechanisms and ductile fracture characteristics of a friction stir processed transformative high entropy alloy, *Acta Mater.* 184 (2020) 164–178.
 - [22] S. Gupta, P. Agrawal, S.S. Nene, R.S. Mishra, Friction stir welding of γ -fcc dominated metastable high entropy alloy: microstructural evolution and strength, *Scripta Mater.* 204 (2021) 114161.
 - [23] W. Wang, W.Z. Mu, D.W. Wei, H.L. Wu, L.B. Yu, T. Jonsson, H. Larsson, H.H. Mao, High corrosion resistance duplex fcc plus hcp cobalt based entropic alloys: an experimental and theoretical investigation, *Mater. Des.* 223 (2022) 111166.
 - [24] J.K. Wang, Y.S. Chen, Y.H. Zhang, Y.C. Zhang, J.J. Li, J. Liu, Y. Liu, W.Z. Li, Microstructure evolution and acid corrosion behavior of $\text{CoCrFeNiCu}_{1-x}\text{Mo}_x$ high-entropy alloy coatings fabricated by coaxial direct laser deposition, *Corrosion Sci.* 198 (2022) 110108.
 - [25] L.A. Chen, Y.S. Lu, Y.T. Lin, Y.L. Lee, Preparation and characterization of cerium-based conversion coating on a $\text{Fe}_{50}\text{Mn}_{30}\text{Co}_{10}\text{Cr}_{10}$ dual-phase high-entropy alloy, *Appl. Surf. Sci.* 562 (2021) 150200.
 - [26] J.L. Lv, Z.H. Tan, T. Liu, The effect of the grain refinement on the corrosion resistance of the CoCrNi medium-entropy alloy in chloride solution, *Intermetallics* 141 (2022) 107423.
 - [27] Z.H. Han, W.N. Ren, J. Yang, A. Tian, Y.Z. Du, G. Liu, R. Wei, G.J. Zhang, Y. Q. Chen, The corrosion behavior of ultra-fine grained CoNiFeCrMn high-entropy alloys, *J. Alloys Compd.* 816 (2020) 152583.
 - [28] K.J. Lu, Z.R. Lei, S. Deng, J.H. Li, T.F. Feng, Z.Y. Luo, X.K. Ma, Synergistic effects of grain sizes on the corrosion behavior and mechanical properties in a metastable high-entropy alloy, *Corrosion Sci.* 225 (2023) 111588.
 - [29] F.J. Cao, G.Q. Huang, W.T. Hou, R.Y. Ni, T. Sun, J.P. Hu, Y.F. Shen, A.P. Gerlich, Simultaneously enhanced strength-ductility synergy and corrosion resistance in submerged friction stir welded super duplex stainless steel joint via creating ultrafine microstructure, *J. Mater. Process. Technol.* 307 (2022) 117660.
 - [30] S.Y. Anaman, S. Ansah, H.H. Cho, M.G. Jo, J.Y. Suh, M.J. Kang, J.S. Lee, S.T. Hong, H.N. Han, An investigation of the microstructural effects on the mechanical and electrochemical properties of a friction stir processed equiautomic CrMnFeCoNi high entropy alloy, *J. Mater. Sci. Technol.* 87 (2021) 60–73.
 - [31] S.S. Nene, K. Liu, M. Frank, R.S. Mishra, R.E. Brennan, K.C. Cho, Z. Li, D. Raabe, Enhanced strength and ductility in a friction stir processing engineered dual phase high entropy alloy, *Sci. Rep.* 7 (1) (2017) 16167.
 - [32] G.Q. Huang, T.H. Chou, S.F. Liu, B. Xiao, J. Ju, J. Gan, T. Yang, P. Zhang, J. X. Yang, C.Y. Lu, F.Q. Meng, Unveiling the microstructure evolution and mechanical properties of submerged friction stir welded joint of fine-grained NiCoCr medium entropy alloy, *Mater. Char.* 200 (2023) 112903.
 - [33] A. Heidarzadeh, T. Saeid, V. Klemm, A. Chabok, Y.T. Pei, Effect of stacking fault energy on the restoration mechanisms and mechanical properties of friction stir welded copper alloys, *Mater. Des.* 162 (2019) 185–197.
 - [34] A. Heidarzadeh, T. Saeid, A comparative study of microstructure and mechanical properties between friction stir welded single and double phase brass alloys, *Mater. Sci Eng A* 649 (2016) 349–358.
 - [35] Z.M. Yang, D.S. Yan, W.J. Lu, Z.M. Li, A TWIP-TRIP quinary high-entropy alloy: tuning phase stability and microstructure for enhanced mechanical properties, *Mater Sci Eng A* 801 (2021) 140441.
 - [36] C. Hu, C.P. Huang, Y.X. Liu, A. Perlade, K.Y. Zhu, M.X. Huang, The dual role of TRIP effect on ductility and toughness of a medium Mn steel, *Acta Mater.* 245 (2023) 118629.
 - [37] C.L. Zhang, L.F. Huang, S.X. Li, K. Li, S.Y. Lu, J.F. Li, Improved corrosion resistance of laser melting deposited CoCrFeNi -series high-entropy alloys by Al addition, *Corrosion Sci.* 225 (2023) 111599.
 - [38] H. Luo, S.W. Zou, Y.H. Chen, Z.M. Li, C.W. Du, X.G. Li, Influence of carbon on the corrosion behaviour of interstitial equiautomic CoCrFeMnNi high-entropy alloys in a chlorinated concrete solution, *Corrosion Sci.* 163 (2020) 108287.

- [39] Z.M. Pan, H. Luo, Q.C. Zhao, H.X. Cheng, Y. Wei, X.F. Wang, B.W. Zhang, X.G. Li, Tailoring microstructure and corrosion behavior of CoNiAl_x medium entropy alloys via Al addition, *Corrosion Sci.* 207 (2022) 110570.
- [40] Z.Q. Yang, A.B. Ma, B.Q. Xu, J.H. Jiang, J.P. Sun, Corrosion behavior of AZ91 Mg alloy with a heterogeneous structure produced by ECAP, *Corrosion Sci.* 187 (2021) 109517.
- [41] F. Weng, Y.X. Chew, W.K. Ong, Y.J. Man, S. Sui, C.L. Tan, F.L. Ng, M.H. Goh, G. J. Bi, Enhanced corrosion resistance of laser aided additive manufactured CoCrNi medium entropy alloys with oxide inclusion, *Corrosion Sci.* 195 (2022) 109965.
- [42] Q.Y. Fu, C. Wang, C.C. Wu, Y. Wu, X.J. Dai, W.H. Jin, B.S. Guo, M. Song, W. Li, Z. T. Yu, Investigating the combined effects of wide stacking faults and grain size on the mechanical properties and corrosion resistance of high-purity Mg, *J. Alloys Compd.* 927 (2022) 167018.
- [43] M.M. Zhao, H.Y. Wu, B. Zhang, J.N. Lu, L.X. Du, Effect of Cr-rich carbide precipitates on austenite stability and consequent corrosion behavior of ultrafine-grained 304 stainless steel produced by cryogenic rolling and annealing treatment, *Mater. Char.* 195 (2023) 112553.
- [44] X.M. Wei, L.J. Zhang, F.Y. Zhang, C.Z. Zhang, Q.X. Jia, K. Sun, D.T. Duan, H. Jiang, G. Li, Effect of carbon addition on the microstructure and corrosion resistance of the CoCrFeNi high-entropy alloy, *Corrosion Sci.* 231 (2024) 111965.
- [45] J.M. Wang, H. Jiang, X.X. Chang, L.J. Zhang, H.X. Wang, L. Zhu, S.X. Qin, Effect of Cu content on the microstructure and corrosion resistance of AlCrFeNi₃Cu_x high entropy alloys, *Corrosion Sci.* 221 (2023) 111313.
- [46] F. Sui, T. An, S.Q. Zheng, L.Q. Chen, S.Y. Li, Influence of effective strain on the corrosion behavior of nickel-based GH4710 superalloy in chloride solutions, *Corrosion Sci.* 204 (2022) 110386.
- [47] M.Q. Sun, J. Yang, Z.B. Wang, Y.G. Zheng, Effect of coexistence of sulfate reducing bacteria and nitrate reducing bacteria on the under-deposit corrosion of carbon steel, *Corrosion Sci.* 231 (2024) 111958.
- [48] Z. Wang, J. Jin, G.H. Zhang, X.H. Fan, L. Zhang, Effect of temperature on the passive film structure and corrosion performance of CoCrFeMoNi high-entropy alloy, *Corrosion Sci.* 208 (2022) 110661.
- [49] Z. Wang, Z. Feng, L. Zhang, Effect of high temperature on the corrosion behavior and passive film composition of 316 L stainless steel in high H₂S-containing environments, *Corrosion Sci.* 174 (2020) 108844.
- [50] F. Yuan, G.Y. Wei, S.R. Gao, S.Y. Lu, H.S. Liu, S.X. Li, X.F. Fang, Y.B. Chen, Tuning the pitting performance of a Cr-13 type martensitic stainless steel by tempering time, *Corrosion Sci.* 203 (2022) 110346.
- [51] H. Luo, Z.M. Li, A.M. Mingers, D. Raabe, Corrosion behavior of an equiatomic CoCrFeMnNi high-entropy alloy compared with 304 stainless steel in sulfuric acid solution, *Corrosion Sci.* 134 (2018) 131–139.
- [52] D.D. Macdonald, Reflections on the history of electrochemical impedance spectroscopy, *Electrochim. Acta* 51 (8–9) (2006) 1376–1388.
- [53] R.W. Fonda, J.F. Bingert, Texture variations in an aluminum friction stir weld, *Scripta Mater.* 57 (2007) 1052–1055.
- [54] M.M. Zhao, H.Y. Wu, J.N. Lu, G.S. Sun, L.X. Du, Effect of grain size on mechanical property and corrosion behavior of a metastable austenitic stainless steel, *Mater. Char.* 194 (2022) 112360.
- [55] C.W. Lu, Y.S. Lu, Z.H. Lai, H.W. Yen, Y.L. Lee, Comparative corrosion behavior of Fe₅₀Mn₃₀Co₁₀Cr₁₀ dual-phase high-entropy alloy and CoCrFeMnNi high-entropy alloy in 3.5 wt% NaCl solution, *J. Alloys Compd.* 842 (2020) 155824.
- [56] S.S. Nene, M. Frank, K. Liu, S. Sinha, R.S. Mishra, B.A. McWilliams, K.C. Cho, Corrosion-resistant high entropy alloy with high strength and ductility, *Scripta Mater.* 166 (2019) 168–172.
- [57] J. Han, X.J. Li, A.Y. Gerard, P. Lu, J.E. Saal, G.S. Frankel, K. Ogle, J.R. Scully, Potential dependent Mn oxidation and its role in passivation of Ni₃₈Fe₂₀Cr₂₂Mn₁₀Co₁₀ multi-principal element alloy using multi-element resolved atomic emission spectroelectrochemistry, *J. Electrochim. Soc.* 168 (5) (2021) 051508.
- [58] K. Park, H. Kwon, Effects of Mn on the localized corrosion behavior of Fe–18Cr alloys, *Electrochim. Acta* 55 (9) (2010) 3421–3427.
- [59] Q.C. Zhao, Z.M. Pan, X.F. Wang, H. Luo, Y. Liu, X.G. Li, Corrosion and passive behavior of Al_xCrFeNi_{3-x} (x=0.6, 0.8, 1.0) eutectic high entropy alloys in chloride environment, *Corrosion Sci.* 208 (2022) 110666.
- [60] P.C. Cui, Z.J. Bao, Y. Liu, F. Zhou, Z.H. Lai, Y. Zhou, J.C. Zhu, Corrosion behavior and mechanism of dual phase Fe_{1.125}Ni_{1.06}CrAl high entropy alloy, *Corrosion Sci.* 201 (2022) 110276.